PHYSICAL REVIEW APPLIED **9,** 044004 (2018)

Electromigration-Induced Surface Drift and Slit Propagation in Polycrystalline Interconnects: Insights from Phase-Field Simulations

Arnab Mukherjee,[1,2,*] Kumar Ankit,[3] Michael Selzer,[1,2] and Britta Nestler[1,2]
[1]*Institute of Materials and Processes, Karlsruhe University of Applied Sciences,*
Moltkestraße 30, 76133 Karlsruhe, Germany
[2]*Institute of Applied Materials–Computational Materials Science,*
Karlsruhe Institute of Technology, Straße am Forum 7, 76131 Karlsruhe, Germany
[3]*School for Engineering of Matter, Transport and Energy, Arizona State University,*
551 East Tyler Mall, Tempe, Arizona 85287, USA

(Received 4 July 2017; revised manuscript received 25 December 2017; published 4 April 2018)

We employ the phase-field method to assess electromigration (EM) damage in wide polycrystalline interconnects due to grain-boundary grooving. An interplay of surface and grain-boundary diffusion is shown to drastically influence the mode of progressive EM damage. Rapid atomic transport along the surface leads to shape-preserving surface drift reminiscent of Blech drift-velocity experiments. On the other hand, a comparatively faster grain-boundary transport localizes the damage, resulting in the proliferation of intergranular slits with a shape-preserving tip. At steady state, the two regimes exhibit exponents of 1 and 3/2, respectively, in Black's law. While surface drift obeys an inverse scaling with grain size, slits exhibit a direct relationship at small sizes, with the dependence becoming weaker at larger ones. Furthermore, we explain the influence of curvature- or EM-mediated healing fluxes running along the surface on groove replenishment. Insights derived from phase-field simulations of EM in bicrystals are extended to investigate the multiphysics of mixed-mode damage of a polycrystalline interconnect line that is characterized by a drift of small grain surfaces, slit propagation, and coarsening. The triple and quadruple junctions are identified as prominent sites of failure.

DOI: 10.1103/PhysRevApplied.9.044004

I. INTRODUCTION

Electromigration (EM)-induced damage manifests in various forms, which can be broadly classified into one of the following categories:

(a) The most commonly observed damage is thinning of large areas of the test piece typically observed in the SEM images of damaged lines after accelerated EM testing [1,2]. A similar mode of damage was observed in the seminal drift-velocity experiments of Blech and Kinsbron [3] and thereafter [4–6].

(b) The second form of damage commences through voiding, typically at sites of nonvanishing (positive) flux divergence [7]. The nucleated voids can evolve along the line preserving its shape or can transform into fingerlike slits [8,9]. Slit growth may be transgranular [10–13] or along the grain boundaries (intergranular) [14–16].

(c) The third damage mode occurs as a result of negative flux divergence leading to mass accumulation. The material extrusions, known as hillocks, lead to failure due to short circuiting between neighboring interconnect levels [17–19].

EM damage by grain-boundary (GB) grooving is one such mechanism which encompasses all of the aforementioned damage manifestations [20]. Grooves can initiate where the GBs intersect a free surface [21]. Accelerated grooving can also lead to slit propagating along GBs or hole formation at the substrate. While voids and slits orginating at grain triple junctions require nucleation in the form of vacancy accumulation, those initiating from GB grooves proceed at any level of vacancy accumulation and preclude the need of any nucleation events [7].

Furthermore, the interplay of various diffusion paths during grooving can also influence the mode of progressive EM damage [22,23]. Polycrystalline metallic lines are characterized by a number of potential diffusional pathways which include the lattice, GBs, and surface and interphase boundaries between the film substrate or film dielectric layers, amongst others [22,24–26]. At typical operational conditions ($< 450\,^{\circ}\mathrm{C}$), bulk diffusivity is negligible, rendering only surfaces and GBs as the potential diffusion pathways.

In bamboo-type lines, where $w \ll d$, w is the linewidth and d is the average grain size, the average orientation

---

[*] muar0002@hs-karlsruhe.de

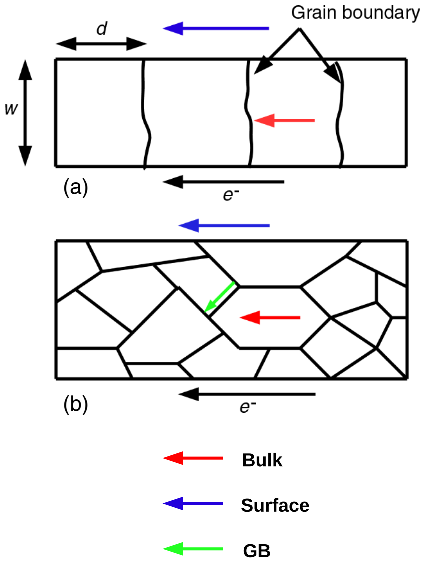

FIG. 1. Schematic illustration depicting various EM pathways in (a) a bamboo-type line and (b) a wide polycrystalline line, where d represents the average grain size and w the linewidth. Surfaces are the predominant EM pathway in the former, while atomic transport proceeds through concurrent surface and GB diffusion in the latter.

of GBs is perpendicular to the electric field, as shown in Fig. 1(a), thus rendering this path moot. Thus, damage proceeds through the surface EM. On the contrary, in wide polycrystalline line where $w > d$, GBs form a continuous network [Fig. 1(b)] and EM occurs via a combination of surface and GB diffusion [1,22]. Therefore, a successful assessment of damage modes during GB grooving, in principle, must account for the disparate pathways in the sample.

Building on our recent work [27], we employ a phase-field method to explore the role of the surface and the GB as possible EM pathways during GB grooving in wide polycrystalline line. The results reveal that the concurrent surface and GB transport can drastically alter the damage modes and subsequent damage propagation depending upon the rate-limiting transport mechanism. This paper is organized as follows. In Sec. II, we describe the phase-field model and a bicrystalline simulation test setup. We then present the numerical simulation results of damage initiation at GB grooves corresponding to the two rate-limiting transport mechanisms in Sec. III. Synergy between our numerical findings and previous analytical and experimental observations is also discussed. Furthermore, implications of grain size distribution and coarsening on the damage initiation in polycrystalline interconnects are highlighted. Section IV concludes the article.

II. PHASE-FIELD MODEL

The theoretical model was already presented in our previous work [27]; however, we recapitulate the free-energy functional and the evolution equations for brevity. The starting point of the thermodynamic state of the system is a free-energy functional depending on a set of order parameters and their respective gradients to describe the interconnect microstructure. The functional is written as

$$F = \int_V f(\rho, \eta_i) + \kappa_\rho |\nabla \rho|^2 + \kappa_\eta \sum_{i=1}^{N} |\nabla \eta_i|^2 dV. \tag{1}$$

A conserved order parameter ρ, which in the present case is the scaled density, distinguishes the interconnect and the underlayer domain. A set of nonconserved order parameters η_i is used to demarcate various grain orientation of the interconnect such that the ith grain is described by $\eta_i = 1$ and $\eta_j = 0 \forall j \neq i$. The bulk free-energy density $f(\rho, \eta_i)$ is a Landau-type polynomial selected to be of the form which results in $(N+1)$ minima in $(\rho, \eta_i, \eta_j) = (1,1,0), (1,0,1), (0,0,0)$ corresponding to the N interconnect grains and the underlayer domain [27,28].

The conserved order parameter ρ is described by the modified Cahn-Hilliard equation as [29]

$$\frac{\partial \rho}{\partial t} = \nabla \cdot [M(\rho, \eta_i) \nabla(\mu + ze\phi)], \tag{2}$$

where the motion of diffusing species is governed by the gradient of chemical and electrical potentials. ze is the effective valence of the diffusing species, which is a sum of the contributions from electrostatic and wind forces. To restrict (or enhance) the diffusion in the narrow regions of the interface such that the interface motion corresponding to the sharp interface limit is recovered, we derive ideas from the scalar mobility formalism with a biquadratic and quadratic polynomial in ρ and η_i, respectively, which is necessary to suppress the bulk-diffusion contribution [28,30].

The temporal evolution of the nonconserved order parameter η_i is governed by the Allen-Cahn equation [31],

$$\frac{\partial \eta_i}{\partial t} = -L_\eta \left(\frac{\partial f(\rho, \eta_i)}{\partial \eta_i} - 2\kappa_\eta \nabla^2 \eta_i \right). \tag{3}$$

Additionally, we rule out any charge accumulation by solving a coupled Laplace equation,

$$\nabla \cdot [\sigma(\rho) \nabla \phi] = 0, \tag{4}$$

where the conductivity, $\sigma(\rho)$, is linearly interpolated between the metal interconnect and the underlayer domain.

A bicrystalline configuration comprising a periodic array of columnar grains with period $2L$, where L is the grain size, as shown in Fig. 2, is selected which is reminiscent of the experimental setup designed by Blech [3]. GBs in the current setup are aligned parallel to the applied electric field. However, this might not always be the case, as GBs need not be entirely in the direct contact of the electron

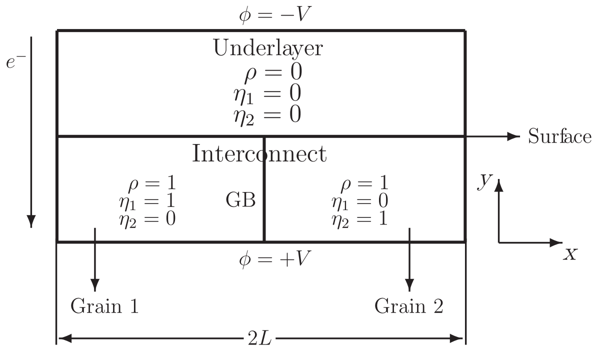

FIG. 2. A schematic illustration of the bicrystalline configuration that is used as an initial condition for the present 2D simulations. Periodic array of interconnect grains with period $2L$, where L is the grain size and the GBs are aligned parallel to the applied electric field.

wind force if they are curved or tilted with respect to the surface. The current setup is motivated by its simplicity and to eliminate effects such as GB migration associated with tilted GBs.

The values of the model parameters used in this work and their relation to the material parameters can be found in the Supplemental Material [32].

III. RESULTS

A. GB diffusion-limited regime (GBDLR)

To begin with, we consider the evolution of grooves when surface diffusion is faster or comparable to the GB diffusion such that $M_S/M_{\mathrm{GB}} = 2$, where M_S and M_{GB} are the atomic mobilities on the surface and the GB, respectively.

1. Morphological evolution

The evolution of the GB grooves at the triple junctions under the concurrent influence of capillarity and EM is shown in Fig. 3(a). A curvature-driven surface diffusion ensues from surface ridges (larger curvature) towards the grain center (smaller curvature). Temporal evolution of the curvature of the grain surface, κ_s, is plotted in Fig. 3(c). Eventually, the tails of the neighboring grooves overlap, elevating the depression at the grain center. This elevation is characterized by a flattening of the curvature profile near the grain center due to the formation of a near-semicircular surface. As soon as the circular arc evolves, the grains start drifting in the direction of the electron wind [Fig. 3(b)], which is reminiscent of the Blech-type drift-velocity experiments [3,4,6]. Overlapping surface curvature profiles observed at larger time steps suggest that the grains preserve their shape as they drift.

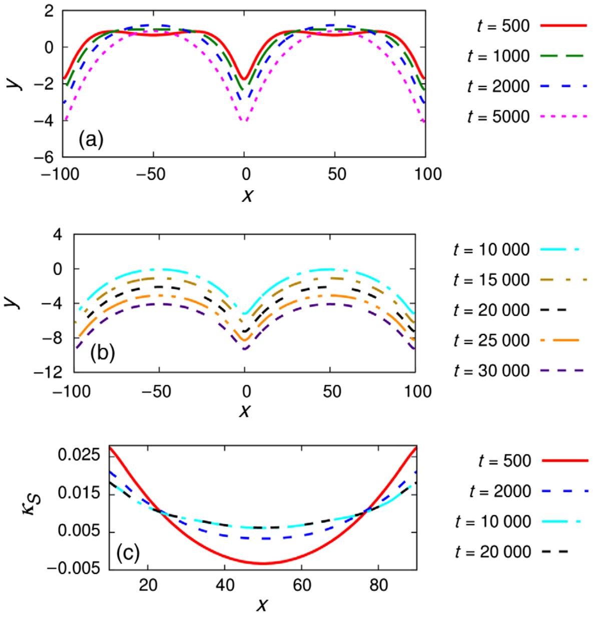

FIG. 3. Temporal evolution of the groove profiles in the GBDLR corresponding to (a) early and (b) late stages. Tails of neighboring grains merge to form circular arcs. Subsequently, the surface drifts in the direction of the electron wind. (c) Curvature along the groove profile. The surface drifts preserving the shape, as apparent from the constancy of curvature.

2. Grooving-drift characteristics

The kinetics of groove displacement is measured from the temporally evolving displacement of the groove root, d_g, relative to the initial flat surface. Two distinct regimes corresponding to the initial grooving and the subsequent drift are discernible in Fig. 4. During the grooving stage, no significant difference in the groove displacement is observed. A nonlinear power fit of the form $k_1 + k_2 t^n$ results in a temporal exponent of $n = 1/4$. The presence of EM does not alter the exponent, which has also been predicted for thermal grooves [21], indicating that the initial stage is predominantly capillary driven. This capillary-mediated grooving is followed by short root deceleration, which is prominent at low field strengths. A steady state is finally attained, as evident from the linear temporal regime.

3. Effect of electric field

During the drifting stage, the velocity can be expressed in terms of a simple mass balance equation as $v = J_{\mathrm{GB}}/L$ [33]

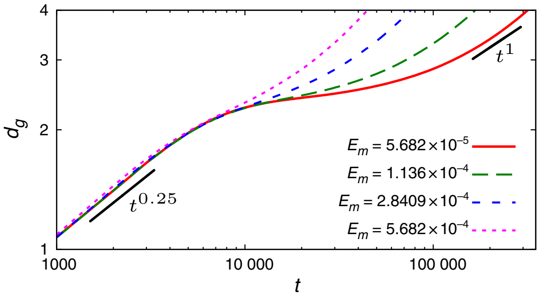

FIG. 4. (a) Displacement-time curve at different field strengths for a grain size of $2L = 200\Delta x$ in the GBDLR. A higher electric field facilitates the steady-state regime.

where J_{GB} is the GB flux and L the grain size. Since $J_{\mathrm{GB}} = M_{\mathrm{GB}} z e E_m$, the velocity scales linearly with the electric field. The steady-state velocity extracted from the slope of the linear regime of a $d_g - t$ curve indeed obeys the linear scaling over a magnitude of the electric field, as shown in Fig. 5(a).

The effect of current density j (or the electric field because of their linear dependence due to Ohm's law) on damage kinetics is expressed according to the modified Black's law [34],

$$t_f = \frac{1}{j^n} \exp\left(\frac{\Delta H}{k_B T}\right), \tag{5}$$

where t_f is the time to failure and ΔH is the activation energy of the process. The above expression can be used to extrapolate the EM test results which are performed at accelerated condition to the service condition. The value of the exponent n sheds light on the mechanism or the rate-limiting step of failure [35]. In the present case, t_f can be expressed as

$$t_f = t_{\mathrm{incub}} + t_{\mathrm{drift}}, \tag{6}$$

where t_{incub} is the incubation time before which drift initiates and t_{drift} is the time elapsed in drift.

Since faster drift corresponds to shorter failure times, i.e., $v \propto 1/t_{\mathrm{drift}}$, the exponent for the second term in the above expression turns out be $n = 1$. Furthermore, as the electric field tends to zero, the incubation time is expected to tend towards infinity. The variation of t_{incub} is plotted in Fig. 5(b), where the data points are fit to the function $t_{\mathrm{incub}} = k_1/(k_2 + E_m)$. As $k_2 \gg E_m$, $t_{\mathrm{incub}} \sim k_1/k_2$ and the curve exhibits a plateau region corresponding to the capillary-dominated regime. On the other hand, at higher field strengths where $E_m \gg k_2$, $t_{\mathrm{incub}} \sim k_1/E_m$, and a linear tail corresponding to the EM-dominated regime can be observed. Thus, in the EM-dominated regime, both stages should result in $n = 1$ in Eq. (5).

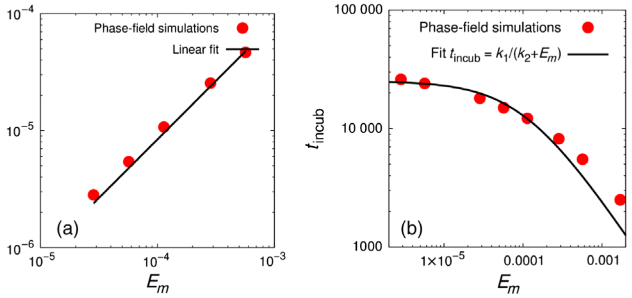

FIG. 5. (a) Scaling of steady-state drift velocity with an electric field in the GBDLR. A linear relationship is obeyed over a magnitude of the electric field. (b) Variation of incubation period with electric field. At low field strengths, a capillary plateau is observed, while at high field strengths a linear regime is exhibited.

4. Effect of grain size

The dependency of grooving and drifting characteristics on the grain size is presented in Fig. 6(a). The root displacement during the initial stage ($t = 100$–400) is higher for smaller grains ($2L = 100\Delta x$) owing to the prominence of curvature-driven flux due to the overlap of neighboring groove tails. Since the grooving stage is prolonged for larger grains, the displacement at the intermittent stage ($t = 500$–$11\,000$) is higher for larger grains, while exhaustion of curvature-driven flux leads to a slowing down of smaller grains. However, since the smaller grain size facilitates the development of a surface arc that initiates drifting, the steady-state regime is attained faster, eventually surpassing the larger grains. The inverse scaling of the grain size during steady-state drift according to the aforementioned mass balance relation is corroborated by the phase-field numerics in Fig. 6(b).

B. Surface diffusion-limited regime (SDLR)

We next move on to the case where transport through the GB is faster than that at the surface, such that $M_S/M_{\mathrm{GB}} = 0.1$. The strength of the electric field is selected to be 1 order of magnitude higher than in the GBDLR. In the following section, we discuss the cases pertaining to large grains and deviations arising due to finite grain sizes sequentially.

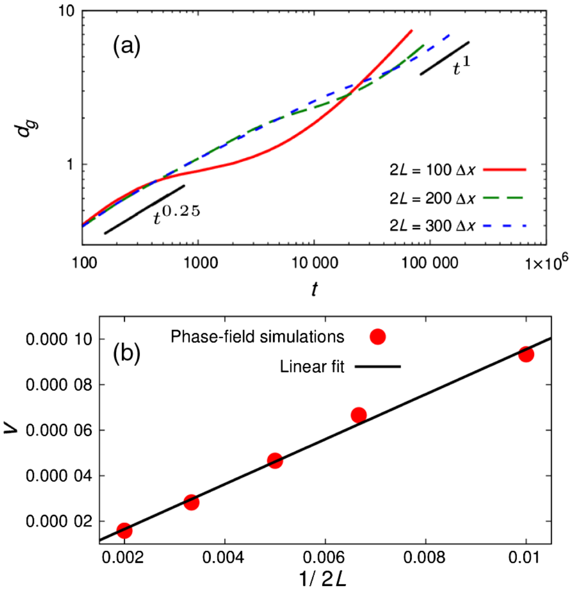

FIG. 6. (a) Displacement-time curve depicting the grain size dependency on drift kinetics in the GBDLR. Smaller grains, owing to the rapid merging of neighboring tails, facilitate surface drift and attainment of the steady state. (b) Velocity dependence on grain size. The steady-state velocity follows an inverse scaling with respect to the grain size. Electric-field strength corresponds to $E_m = 5.6818 \times 10^{-4}$.

1. Morphological evolution

A predominance of GB diffusion accelerates the grooving rate in Fig. 7(a), as compared to Fig. 3(a). As a result of low surface diffusivity and large grain size, any overlap of the neighboring groove tails is found to be absent. The grooves temporally widen, forming a cavity at the root. Ultimately, a narrow, slitlike channel develops [Fig. 7(b)] which then propagates along the GB, preserving its width and shape. A fast GB diffusion flux is responsible for localizing the damage along GB, as opposed to the Blech-type regime, where the entire surface drifts homogeneously. The trailing edge evolves through surface diffusion to form arcs, as observed in Fig. 7(b), and eventually starts drifting. In other words, while the entire surface drifts, conserving its shape when surface diffusion predominates, shape is conserved only near the tip region of the slit in the SDLR. It is also worth noting that the convexity of the groove root is preserved when the surface drifts, as opposed to slit formation, where the root curvature transitions from convex to concave [Fig. 7(c)] during evolution.

2. Slit propagation kinetics

The $d_g - t$ curve corresponding to a different electric field is plotted in Fig. 8. Similar to the Blech regime in Fig. 4, two distinct kinetic regions can be identified. In this case, the transient stage exhibits a faster kinetics evident from the temporal exponent of $3/4$. As the root detaches from the surface to form a slit, it deepens with a steady-state velocity, as evident from the linear exponent in the $d_g - t$ curve. Larger field strengths hasten the transition to a steady state.

3. Effect of electric field

The sharp interface GB grooving model proposed in Refs. [33,36] predicts an $E^{3/2}$ dependency of slit kinetics.

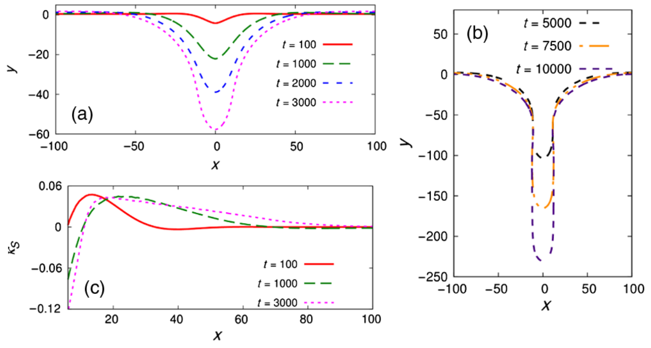

FIG. 7. Temporal evolution of grooves in SDLR at (a) early and (b) late stages. Faster GB transport leads to accelerated grooving, followed by the development of a cavity at the root which eventually forms a channel-like slit that advances along the GB, maintaining a constant width and shape. (c) Curvature profile along the groove. Slit formation changes the curvature of the root from convex to concave. The grain size and electric-field strength corresponds to $2L = 400\Delta x$ and $E_m = 2.3674 \times 10^{-3}$, respectively.

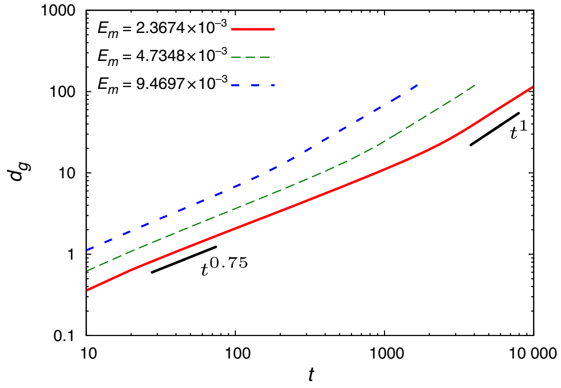

FIG. 8. Displacement-time curve illustrating the kinetics of slit propagation in the SDLR. After an initial growth exponent $3/4$, the slit attains a dynamic steady state.

The velocities computed via present phase-field simulations at different magnitudes of electric-field strength confirm the corresponding scaling law in Fig. 9. Drawing an analogy from the GBDLR, failure in the present case can be expressed as

$$t_f = t_g + t_p, \tag{7}$$

where t_g and t_p correspond to the initial accelerated grooving and slit propagation stages, respectively. The GB grooving model by Rosenberg and Ohring [7] suggests that EM-induced grooving (not slit propagation) leads to hole formation in which the time to failure exhibits an $E_m^{4/3}$ dependence. This relationship can also be inferred from Fig. 8 during the initial stages, where $d_g \propto t^{3/4}$ and the prefactor depends on the magnitude of E_m. If the groove root continues propagating following this temporal law, the $t_g \propto E_m^{4/3}$ value proposed by Rosenberg and Ohring is expected. Thus, while the former (t_g) leads to $n = 4/3$, the latter (t_p) gives rise to $n = 3/2$. Hence, the exponent in Eq. (5) is anticipated to lie between $4/3$ and $3/2$, depending upon the rate-limiting step.

4. Effect of grain size

Traditionally, the sharp interface models analyze the slit dynamics independently once the slit is detached from the

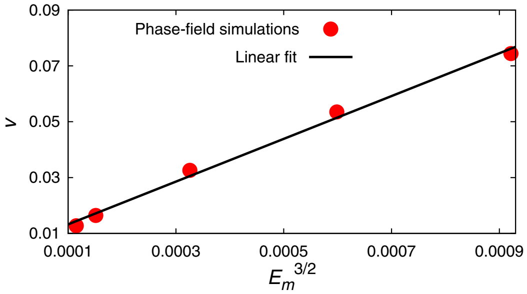

FIG. 9. Velocity dependency on the electric field in the SDLR. A higher electric field leads to fast-propagating slits.

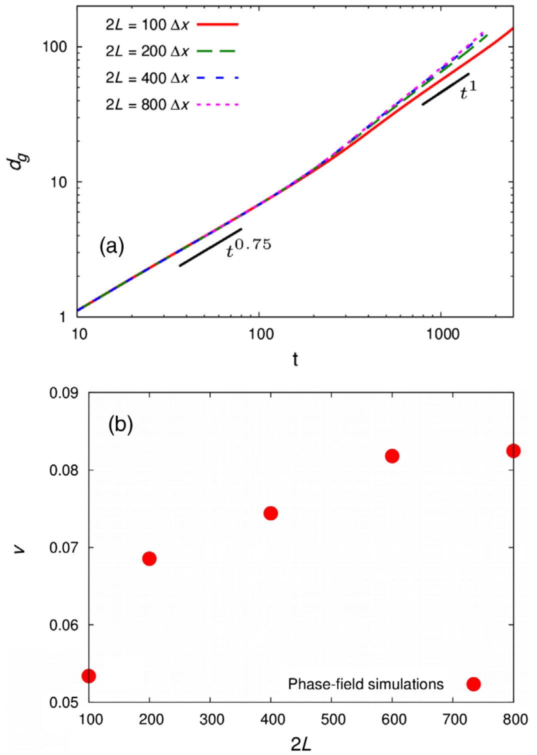

FIG. 10. (a) Displacement-time curve in the SDLR depicting the grain size dependency on slit kinetics. Deviation arises progressively at late stages in order of increasing grain size. (b) Velocity dependence on grain size. Slits originating from smaller grains lead to slower propagation. The dependency becomes weaker as the grain size is increased. The electric-field strength corresponds to $E_m = 9.4697 \times 10^{-3}$.

surface, assuming an idealized geometry such that the slit surface is parabolic while the tip retains an equilibrium dihedral angle and is flat farther away. It does not take into account the influence of the initial grain size on slit kinetics. Our phase-field simulations, on the other hand, nicely capture the nonlinearities associated with slit initiation from GB grooves and subsequent advancement without making any *a priori* assumptions on the slit shape. Hence, the proposition of grain size independence on slit kinetics is easily verified via the present simulations. The $d_g - t$ curve corresponding to different grain sizes is presented in Fig. 10(a). Although any difference in kinetics during the initial stages is indiscernible, deviation arises progressively at later stages in the order of increasing grain size. The overlapping of neighboring groove profiles in the case of smaller grains leads to concomitant surface drift in addition to slit propagation. For the constant voltage setup, this drifting leads to a significant decrease in the GB flux leading to a slower kinetics at later stages. The steady-state velocity corresponding to different grain sizes is plotted in Fig. 10(b). While the influence of small grain size on the slit kinetics is strong, the dependency becomes weaker as the grain size increases due to the absence or delay of simultaneous surface drift.

C. Role of the surface and the GB as the EM pathway

To better assess the role of the surface and the GB as potential EM pathways, we plot the surface and GB flux vectors superimposed on the groove profile. Figure 11(a) corresponds to the GBDLR [Fig. 3(b) at $t = 10\,000$]. While the EM-induced GB flux, J_{GB}^E, leads to groove extension, surface currents replenish the groove. The mechanism of grooving during EM was proposed by Mukherjee *et al.* [27], who attributed the healing flux to surface EM, J_S^E. In this work, the convexity at the root is found to be sustained during homogeneous drift [as in Fig. 3(c)], irrespective of the grain size and strength of the electric field. Hence, the surface current in Fig. 11(a) is due only to J_S^E.

In the SDLR, root concavity [Fig. 6(d)] promotes material transport towards the root. In addition to J_S^E, the curvature-gradient-induced surface flux $J_S^{\nabla\kappa_S}$ also contributes to the healing flux [Fig. 11(b), which corresponds to $t = 3000$ in Fig. 7(a)]. Because of the dual healing mechanism of $J_S^E + J_S^{\nabla\kappa_S}$, surface currents near the root are intense, while they are relatively weak farther away because of the sole effect of J_S^E. The origin of the healing fluxes can therefore be curvature gradient or EM induced or both, depending upon the predominance of capillarity over EM, or vice versa.

Thus, a homogeneous displacement is favored when $J_S^E \gtrapprox J_{\mathrm{GB}}^E$, which is most likely to occur when $M_S/M_{\mathrm{GB}} \gtrapprox 1$ and there are low to moderate field strengths since increasing the electric-field strengths inadvertently increases J_S^E. On the other hand, a groove-to-slit transition results if $J_{\mathrm{GB}}^E \gg (J_S^E + J_S^{\nabla\kappa_S})$, which is preferable, as $M_{\mathrm{GB}}/M_S \gg 1$ and there are high field strengths.

D. Polycrystalline line

The study of the damage of the bicrystalline configuration discussed hitherto, although providing numerous

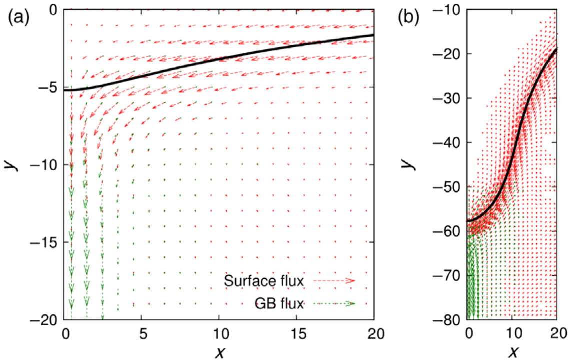

FIG. 11. Surface (red arrows) and GB (green arrows) currents in (a) the GBDLR and (b) the SDLR. While EM-induced surface flux replenishes the groove root in the GBDLR, curvature gradients result in an additional mode of healing mechanism. The magnitude of flux vectors are upscaled for clarity.

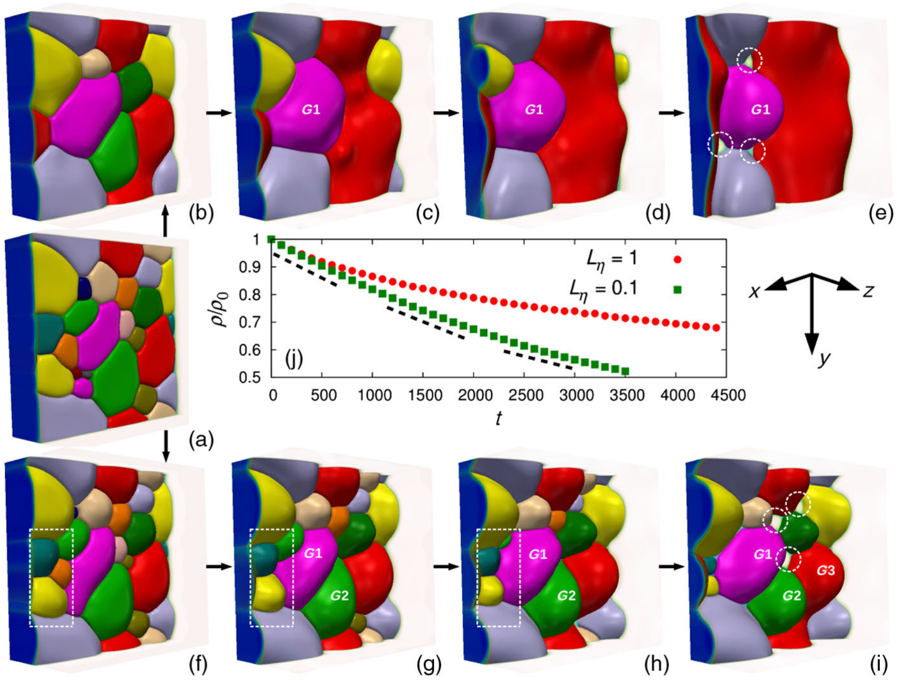

FIG. 12. Damage in a polycrystalline line initiating from a multigrained structure (a) $t = 0$ for high GB mobility ($L_\eta = 1$) at (b) $t = 500$, (c) $t = 1500$, (d) $t = 2500$, (e) $t = 4400$ and low GB mobility ($L_\eta = 0.1$) corresponding to (f) $t = 500$, (g) $t = 1500$, (h) $t = 2500$, and (i) $t = 3500$ in the SDLR. Smaller grains exhibit surface drifting (shown by the white dotted box), while junctions around larger grains exhibit a propensity of slit formation. The triple and quadruple junctions are the preferential sites of failure (the white dotted circles). (j) Temporal evolution of relative density of the interconnect depicting the drift of the polycrystalline line.

fundamental insights, is of limited practical value. In reality, commercial interconnects are polycrystalline (having more than two grains) with a mixed grain size distribution. As a result, curvature-driven grain coarsening can also potentially play a vital role in the initiation of damage. Naturally, in addition to the surface and GB diffusivities, the GB mobility (L_η), which determines the coarsening rate, should also be considered in order to comprehend the damage mechanisms.

In this section, we extend our phase-field model to numerically investigate the damage modes in polycrystalline interconnects. For simplicity, we limit this study to 20 nonconserved order parameters corresponding to grains of different orientations and retain the columnar structure. Practically, such a configuration corresponds to an interconnect line blocked by a large single crystal. Starting with a polycrystalline grain distribution that is generated via a 2D grain growth simulation [Fig. 12(a)], we focus on damage modes that are operative in the SDLR. In the following 3D simulations, the grain mobility L_η is varied between 0.1 and 1.0 to decompose the influence of coarsening on damage proliferation. Every grain orientation is assigned a different color for the sake of clarity.

Upon comparing the number of grains in Figs. 12(b) and 12(f), it is observed that coarsening is enhanced at a larger value of L_η, wherein smaller grains are consumed by larger ones. Concurrently, GB networks, which are a dominant pathway, perish rapidly. GB grooves are clearly visible in both cases, though no noticeable differences in terms of failure initiation can be perceived.

To quantify EM-induced damage, we define the relative density of the interconnect as ρ/ρ_o, where ρ is the instantaneous density and ρ_o is the initial value. As the damage proceeds, this parameter quantifies the amount of drift along the line and the residual trailing edge. The temporal evolution of relative density is plotted in Fig. 12(j). Clearly, in the early stages ($t = 500$), the extent of damage in both of the lines is similar (approximately 10%). However, during later stages, smaller grains survive longer when $L_\eta = 0.1$, which results in a thinning of areas with small grains. As an example, consider the smaller grains on the left edges of Figs. 12(f), 12(g), and 12(h) enclosed in white dashed boxes, which drift faster than their larger neighbors, designated as $G1$ and $G2$ in Figs. 12(g) and 12(h), respectively. On the other hand, larger grains ($G1$) in both cases undergo marginal or almost no drift. This stagnancy is clearly evident in Fig. 12(j) where, at $t = 2500$, the smaller grain sample ($L_\eta = 0.1$) displays a drift of 40%, as compared to 25% in large-grain test piece ($L_\eta = 1$). This finding is in qualitative agreement with those for the bicrystalline configuration, where drift velocity is found to be inversely related to grain size.

For $L_\eta = 1$, where grain coarsening is prevalent, the propensity of slit initiation from the grooves increases with time. However, at a lower L_η ($= 0.1$), the damage proceeds via a mixed mode wherein smaller grains exhibit thinning as slits develop along GB junctions of the larger grains, though the thinning is definitely reduced. This slit propensity is evident in the slowing of the drift of the interconnect in Fig. 12(j). While the drift between $t = 1500$ and $t = 2500$ is around 15%, it is a little less than 10% between $t = 2500$ and $t = 3500$ for the $L_\eta = 0.1$ system. The curve plotted for $L_\eta = 1$ is comparatively flatter due to morphogenesis of the slits, resulting in a large residual trailing edge.

Another consequence of a small GB mobility is that, for the same line length, the time to failure is smaller [$t = 3500$

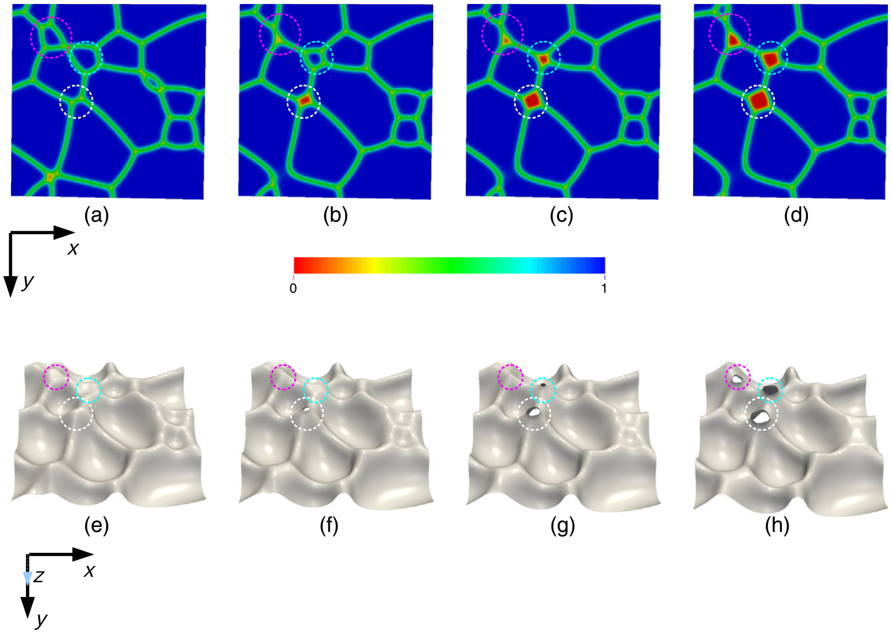

FIG. 13. Temporal evolution of the bottom section of the polycrystalline line showing the predominant failure sites at (a) $t = 2500$, (b) $t = 2900$, (c) $t = 3100$, and (d) $t = 3500$ for $L_\eta = 0.1$. Here, grains illustrated in blue are separated by green GBs. Red denotes the exposed underlayer domain due to hole formation by accelerated GB grooving initiating from the top surface. Temporal evolution of a $\rho = 0.5$ surface contour at (e) $t = 2500$, (f) $t = 2900$, (g) $t = 3100$, and (h) $t = 3500$. Junctions around larger grains (shown in the white dotted circles) are the ones that fail more readily. Dissolution of smaller grains leads to slit merging and subsequent failure (the cyan and magenta dotted circles).

for $L_\eta = 0.1$ in Fig. 12(i), compared to $t = 4400$ for $L_\eta = 1$ in Fig. 12(e)]. Clearly, interconnects with a smaller average grain size possess larger GB networks that accelerate surface drift. For deeper insight, it is worth investigating the primary sites of failure. To track the events that lead to failure, the temporal evolution of the bottom plane of the line corresponding to $L_\eta = 0.1$ is presented in Figs. 13(a)–13(d). To demarcate the grains and GBs, we plot $\Phi = \sum \eta_i^2$, such that $\Phi = 0$ corresponds to the underlayer, $\Phi = 1$ represents the grains of interconnect, and $\Phi = 0.5$ the GBs. Moreover, the $\rho = 0.5$ surface contour is also shown in Figs. 13(e)–13(h).

The first junctions of failure are the ones that are surrounded by the larger grains designated as $G1$, $G2$, and $G3$ in Fig. 12(i) and enclosed inside the white dotted circles in Figs. 13(a), 13(b), 13(e), and 13(f). GBs or junctions of larger grains, while acting as sites where slits initiate, also promote their proliferation, as discussed in Sec. III. Moreover, the triple and quadruple junctions are comparatively more susceptible to damage than the GBs are. For instance, the damage occurs at a faster rate along the quadruple junction when $L_\eta = 0.1$ [Figs. 12(i), 13(b), and 13(f)]. Similarly, in Fig. 12(e) ($L_\eta = 1$), holes form at triple junctions around grain $G1$.

The second predominant failure sites are the grain junctions originating due to dissolution of smaller grains, as shown in Fig. 13 (the magenta and cyan dotted circles), especially if the neighboring grains are large. Smaller grains due to a larger EM surface drift entail large thinning, but, when consumed by neighboring grains, cause slits to merge. This interesting event is nicely captured in Figs. 13(e)–13(h) (by the magenta and cyan dotted circles), where the protruding junctions from the neighborhood of smaller grains approach each other as grain continuously shrinks. Finally, the adjoining slit tips coalesce before evolving in unison.

IV. DISCUSSIONS AND CONCLUDING REMARKS

This work is applicable to polycrystalline lines where GB grooving proceeds via concurrent surface and GB atomic diffusion and EM. Our work comes closest to the experimental study of damage morphology of copper interconnects by Gladkikh *et al.* [1] and McCusker *et al.* [2]. Both the surface condition and the grain size distribution were reported to influence the damage modes. The absence of an overlayer (such as tantalum) which promotes oxidation and the formation of oxide precipitates accelerate slit growth. Both of these observations can be argued based on slow surface diffusion, which concomitantly hinders the healing process which is corroborated by this work. Global thinning of the sample is attributed to small grain size distribution. Surface diffusivity is assumed to be comparable to GB diffusivity (though the exact diffusivity values are not reported) to explain the observed damage modes by comparing the parameters to the GB grooving model in Ref. [33]. The aforementioned observation can also be rationalized on the basis of healing flux highlighted in this work, even in the SDLR. A sufficient value of $(J_S^E + J_S^{\nabla\kappa_S})$ outweighs J_{GB}^E, as a result of which the root detachment phenomenon is not observed. This nondetachment is expected to be observed at smaller grain size and lower electric-field strength.

This work builds upon the analytical theory of Klinger and co-workers [14,33,36] and highlights the importance of curvature gradient- and EM-induced surface healing flux, which was not accounted for in previous investigations [33,36]. Although the scaling laws derived in

Refs. [14,33,36] are well reproduced by the phase-field method, incumbent healing fluxes delay the growth of damage by replenishing the groove root. In addition, we identify a mixed mode of damage in polycrystalline lines wherein smaller grains exhibit thinning, while slits manifest around junctions of larger grains. Grain triple and quadruple junctions are identified as preferential sites of failure.

The model in the present form does not consider the Blech effect. As the sample drifts in the direction of electron wind, mass accumulation at the anode gives rise to back stresses that hinder the EM-induced displacement [4,5]. The timescale on which back-stress gradients develop scales into hours; therefore, our predictions on early-stage damage propagation hold. In addition, the presence of residual or thermal stress [37,38] arising during the fabrication or annealing cycle is not considered. In the present framework, physics of both back-stress accumulation and thermal stress can be incorporated by solving a complete elastic boundary-value problem [39,40] or through an atomistically informed formalism of phase-field crystal (PFC) models [41]. Moreover, phenomena such as void nucleation at the cathode end and crystalline defects such as triple junctions and GBs can also be studied using PFC models. Here, it is important to mention that the genesis of slits in the SDLR, in this work, is not a nucleation phenomenon; rather, it is the manifestation of accelerated GB grooving. While void nucleation results in an exponent of $n = 2$ in Black's law (which is faithfully reproduced by PFC models), this work elucidates the damage in the form of global thinning and an intergranular slit initiated from GB grooves leading to $n = 1$ and $n = 3/2$, respectively, in steady state. PFC studies, however, are currently limited to bulk-diffusion regimes.

Another assumption utilized in this work is the isotropy in the surface adatom mobility. However, most commercial interconnects are face-centered-cubic (fcc) metals which are characterized by a strong diffusional anisotropy. This effect can be included by introducing crystallographic direction dependence in surface atomic mobility (M_S) [42] as $M(\rho,\eta_i) = M_S(\rho)[1 + \delta \cos k(\theta + \psi)]$, where δ denotes the anisotropy strength, $\theta = \tan^{-1}(\rho_y/\rho_x)$ is the angle between normal to the surface ($\boldsymbol{\nabla}\rho$) and the x axis, and ψ represents the misorientation angle between the fastest diffusion direction and the x axis. k depicts the number of diffusion paths on a crystalline plane. For fcc metals, $k = 2$, 4, 6 corresponds to the $\{110\}$, $\{100\}$, and $\{111\}$ planes, respectively. The presence of diffusional anisotropy can lead to richness in the dynamics of GB grooving and slit formation in polycrystalline lines, as has been previously demonstrated for bamboo-type lines [43] and single-crystal islands [44–46]. GB diffusional anisotropy can also be modeled along similar lines.

Insights gained from this work can be easily extrapolated to other technologically relevant configurations, such as near bamboo lines or slit initiation and growth along the sidewalls (e.g., the top surface in Fig. 1) transverse to the line. While EM-induced GB transport drains the root (as long as the GB is tilted) similar to what we observe in the present configurations, the EM-induced surface healing flux is unidirectional. This unidirectional healing will eventually result in the formation of asymmetric grooves with a mass-depleted leeward side while the mass accumulates on the windward side [43,47,48]. However, the steady-state morphology and the dynamics of the slits are anticipated to be consistent with the ones presented in this article, as these characteristics arise solely on dimensional arguments.

ACKNOWLEDGMENTS

The authors acknowledge financial support from the ministry of the state Baden-Wuerttemberg through the initiative "Mittelbau," from "Bundesministerium für Wirtschaft und Energie" within the project "KerSOLife100" and from the Helmholtz Association through the project "KIT-Geothermal integration initiative" within the program "RE-renewable energies." K. A. acknowledges start-up financial support from the College of Engineering at Arizona State University.

[1] A. Gladkikh, M. Karpovski, A. Palevski, and Yu. S. Kaganovskii, Effect of microstructure on electromigration kinetics in Cu lines, J. Phys. D **31**, 1626 (1998).

[2] N. D. McCusker, H. S. Gamble, and B. M. Armstrong, Surface electromigration in copper interconnects, Microelectron. Reliab. **40**, 69 (2000).

[3] I. A. Blech and E. Kinsbron, Electromigration in thin gold films on molybdenum surfaces, Thin Solid Films **25**, 327 (1975).

[4] Illan A. Blech, Electromigration in thin aluminum films on titanium nitride, J. Appl. Phys. **47**, 1203 (1976).

[5] I. A. Blech and K. L. Tai, Measurement of stress gradients generated by electromigration, Appl. Phys. Lett. **30**, 387 (1977).

[6] E. Kinsbron, I. A. Blech, and Y. Komem, The threshold current density and incubation time to electromigration in gold films, Thin Solid Films **46**, 139 (1977).

[7] R. Rosenberg and M. Ohring, Void formation and growth during electromigration in thin films, J. Appl. Phys. **42**, 5671 (1971).

[8] O. Kraft and E. Arzt, Electromigration mechanisms in conductor lines: Void shape changes and slit-like failure, Acta Mater. **45**, 1599 (1997).

[9] Eduard Arzt, Oliver Kraft, William D. Nix, and J. E. Sanchez, Jr., Electromigration failure by shape change of voids in bamboo lines, J. Appl. Phys. **76**, 1563 (1994).

[10] Z. Suo, W. Wang, and M. Yang, Electromigration instability: Transgranular slits in interconnects, Appl. Phys. Lett. **64**, 1944 (1994).

[11] M. Rauf Gungor and Dimitrios Maroudas, Theoretical analysis of electromigration-induced failure of metallic thin

films due to transgranular void propagation, J. Appl. Phys. **85**, 2233 (1999).

[12] Yao Yao, Leon M. Keer, and Morris E. Fine, Electromigration effect on pancake type void propagation near the interface of bulk solder and intermetallic compound, J. Appl. Phys. **105**, 063710 (2009).

[13] Yao Yao, Yuexing Wang, Leon M. Keer, and Morris E. Fine, An analytical method to predict electromigration-induced finger-shaped void growth in SnAgCu solder interconnect, Scr. Mater. **95**, 7 (2015).

[14] L. M. Klinger, X. Chu, W. W. Mullins, and C. L. Bauer, Grain-boundary slit propagation in an electric field, J. Appl. Phys. **80**, 6670 (1996).

[15] Chao-Yuan Liu, Sanboh Lee, and Tze-jer Chuang, Grain boundary crack growth in interconnects with an electric current, Mater. Sci. Eng. B **86**, 101 (2001).

[16] Hao-Wen Hsueh, Fei-Yi Hung, and Truan-Sheng Lui, A study on electromigration-inducing intergranular fracture of fine silver alloy wires, Appl. Phys. Lett. **110**, 031902 (2017).

[17] A. Gladkikh, Y. Lereah, E. Glickman, M. Karpovski, A. Palevski, and J. Schubert, Hillock formation during electromigration in Cu and Al thin films: Three-dimensional grain growth, Appl. Phys. Lett. **66**, 1214 (1995).

[18] J. A. Nucci, A. Straub, E. Bischoff, E. Arzt, and C. A. Volkert, Growth of electromigration-induced hillocks in Al interconnects, J. Mater. Res. **17**, 2727 (2002).

[19] Min-Seung Yoon, Min-Ku Ko, Oh-Han Kim, Young-Bae Park, William D. Nix, and Young-Chang Joo, In situ observation of electromigration in eutectic SnPb solder lines: Atomic migration and hillock formation, J. Electron. Mater. **36**, 562 (2007).

[20] Milton Ohring, Electromigration damage in thin films due to grain boundary grooving processes, J. Appl. Phys. **42**, 2653 (1971).

[21] William W. Mullins, Theory of thermal grooving, J. Appl. Phys. **28**, 333 (1957).

[22] C.-K. Hu, R. Rosenberg, and K. Y. Lee, Electromigration path in Cu thin-film lines, Appl. Phys. Lett. **74**, 2945 (1999).

[23] E. Glickman and M. Nathan, On the unusual electromigration behavior of copper interconnects, J. Appl. Phys. **80**, 3782 (1996).

[24] J. R. Lloyd and J. J. Clement, Electromigration in copper conductors, Thin Solid Films **262**, 135 (1995).

[25] A. Gladkikh, Y. Lereah, M. Karpovski, A. Palevski, and Yu. S. Kaganovskii, in *Symposium K—Advanced Metallization for Future ULSI*, edited by K.-N. Tu, MRS Symposia Proceedings No. 427 (Materials Research Society, Pittsburgh, 1996), p. 121.

[26] C. K. Hu, K. Y. Lee, L. Gignac, and R. Carruthers, Electromigration in 0.25 μm wide Cu line on W, Thin Solid Films **308**, 443 (1997).

[27] Arnab Mukherjee, Kumar Ankit, Rajdip Mukherjee, and Britta Nestler, Phase-field modeling of grain-boundary grooving under electromigration, J. Electron. Mater. **45**, 6233 (2016).

[28] Rajdip Mukherjee, Tamoghna Chakrabarti, Erumpukuthickal Ashok Anumol, Thennathur Appandairajan Abinandanan, and Narayanan Ravishankar, Thermal stability of spherical nanoporous aggregates and formation of hollow structures by sintering a phase-field study, ACS Nano **5**, 2700 (2011).

[29] John W. Cahn and John E. Hilliard, Free energy of a nonuniform system. I. Interfacial free energy, J. Chem. Phys. **28**, 258 (1958).

[30] Alpha Albert Lee, Andreas Munch, and Endre Suli, Sharp-interface limits of the Cahn-Hilliard equation with degenerate mobility, SIAM J. Appl. Math. **76**, 433 (2016).

[31] Samuel M. Allen and John W. Cahn, A microscopic theory for antiphase boundary motion and its application to antiphase domain coarsening, Acta Metall. **27**, 1085 (1979).

[32] See Supplemental Material at http://link.aps.org/supplemental/10.1103/PhysRevApplied.9.044004 for a discussion on the selection of numerical parameters and its relation to material parameters.

[33] L. M. Klinger, E. E. Glickman, V. E. Fradkov, W. W. Mullins, and C. L. Bauer, Extensions of thermal grooving for arbitrary grain-boundary flux, J. Appl. Phys. **78**, 3833 (1995).

[34] James R. Black, Electromigration failure modes in aluminum metallization for semiconductor devices, Proc. IEEE **57**, 1587 (1969).

[35] J. R. Lloyd, Black's law revisited nucleation and growth in electromigration failure, Microelectron. Reliab. **47**, 1468 (2007).

[36] E. E. Glickman and L. M. Klinger, in *Symposium T—Materials Reliability in Microelectronics V*, edited by W. F. Filter, K. Gadepally, A. L. Greer, A. S. Oates, and R. Rosenberg, MRS Symposia Proceedings No. 391 (Materials Research Society, Pittsburgh, 1995), p. 243.

[37] Seung-Hyun Rhee, Yong Du, and Paul S. Ho, Thermal stress characteristics of Cu/oxide and Cu/low-k submicron interconnect structures, J. Appl. Phys. **93**, 3926 (2003).

[38] I. C. Noyan, Conal E. Murray, Jay S. Chey, and Charles C. Goldsmith, Finite size effects in stress analysis of interconnect structures, Appl. Phys. Lett. **85**, 724 (2004).

[39] Deepali N. Bhate, Ashish Kumar, and Allan F. Bower, Diffuse interface model for electromigration and stress voiding, J. Appl. Phys. **87**, 1712 (2000).

[40] Nan Wang and Nikolas Provatas, Role of Stress-Driven Interfacial Instability in the Failure of Confined Electric Interconnects, Phys. Rev. Applied **7**, 024032 (2017).

[41] Nan Wang, Kirk H. Bevan, and Nikolas Provatas, Phase-Field-Crystal Model for Electromigration in Metal Interconnects, Phys. Rev. Lett. **117**, 155901 (2016).

[42] Mohan Mahadevan and R. Mark Bradley, Simulations and theory of electromigration-induced slit formation in unpassivated single-crystal metal lines, Phys. Rev. B **59**, 11037 (1999).

[43] Oncu Akyildiz and Tarik Omer Ogurtani, Grain boundary grooving induced by the anisotropic surface drift diffusion driven by the capillary and electromigration forces: Simulations, J. Appl. Phys. **110**, 043521 (2011).

[44] Philipp Kuhn, Joachim Krug, Frank Hausser, and Axel Voigt, Complex Shape Evolution of Electromigration-Driven Single-Layer Islands, Phys. Rev. Lett. **94**, 166105 (2005).

[45] Ashish Kumar, Dwaipayan Dasgupta, and Dimitrios Maroudas, Complex Pattern Formation from Current-Driven Dynamics of Single-Layer Homoepitaxial Islands

on Crystalline Conducting Substrates, Phys. Rev. Applied **8**, 014035 (2017).

[46] Dwaipayan Dasgupta, Ashish Kumar, and Dimitrios Maroudas, Analysis of current-driven oscillatory dynamics of single-layer homoepitaxial islands on crystalline conducting substrates, Surf. Sci. **669**, 25 (2018).

[47] Tarik Omer Ogurtani and Oncu Akyildiz, Grain boundary grooving and cathode voiding in bamboo-like metallic interconnects by surface drift diffusion under the capillary and electromigration forces, J. Appl. Phys. **97**, 093520 (2005).

[48] Supriyo Chakraborty, Master's thesis, Indian Institute of Science, 2016.